Synergistic Coupling of Multiphase Transport and Chemical Capture Enables High-Rate Plasma Nitrogen Fixation

Qiuyun Lu,[†] Mohammadjavad Palimi,[†] Minggang Xie,[†] Hongbo Shi,[‡] Bowei Li,[¶] Yunwei Ryan Li,[¶] Zhi Li,[†] and Xuehua Zhang[*,†]

[†]*Department of Chemical and Materials Engineering, University of Alberta, Edmonton, Alberta T6G 1H9, Canada*

[‡]*Research Center of Fluid Machinery Engineering and Technology, Jiangsu University, Zhenjiang, 212013, Jiangsu, China*

[¶]*Department of Electrical Computer Engineering University of Alberta, Edmonton, Alberta T6G 1H9, Canada*

E-mail: xuehua.zhang@ualberta.ca

1. Experimental methods

1.1 Chemicals and materials

Ultrapure water (Milli-Q) was obtained from a water purification unit (Merck, Germany); measured at room temperature (25 °C), it possessed an electrical conductivity of 3.3 μS cm^{-1} and a pH of 5.5. Sodium hydroxide (NaOH, 95%, Sigma-Aldrich) was used to adjust the pH of the water matrix for MB-CPA experiments. The reagents used for determining the concentrations of NO_2^-, NO_3^-, and H_2O_2 in the aqueous solution included titanium(IV) oxysulfate-sulfuric acid ($TiOSO_4$), Griess reagent, and hydrochloric acid (HCl, 1 M), all of which were purchased from Sigma-Aldrich.

For EPR analysis, TEMPOL (4-hydroxy-2,2,6,6-tetramethylpiperidine-1-oxyl, $\geq$ 95%), catalase (from bovine liver, 2000–5000 $\mathrm{U\,mg^{-1}}$ protein), superoxide dismutase (SOD, from bovine erythrocytes, $\geq$ 3000 $\mathrm{U\,mg^{-1}}$ protein), and uric acid (analytical standard) were obtained from Sigma-Aldrich (Canada). All solutions were freshly prepared immediately before use. Stock solutions of TEMPOL (50 mM), catalase (100,000 $\mathrm{U\,mL^{-1}}$), and SOD (10,000 $\mathrm{U\,mL^{-1}}$) were prepared in ultrapure water and stored at $-18\,^{\circ}\mathrm{C}$ in the dark. All stock solutions were thawed only once on ice before experiments and used within 24 h. A sodium urate stock solution (50 mM) was freshly prepared on the day of use by dissolving uric acid in 0.2 M NaOH until the solution became clear. All glassware was rinsed thoroughly with ultrapure water and kept tightly capped to minimize CO_2 absorption prior to use.

1.2 Experimental setup and treatment conditions

The DBD plasma-assisted MB-CPA setup includes a peristaltic pump (WT600-4F, Longer, China) to ensure uniform water circulation within the container, promoting the even distribution of plasma-generated reactive species throughout the aqueous solution. The DBD plasma reactor is powered by a high-voltage generator capable of delivering an input power of 100 W with an adjustable AC frequency of 0 to 10 kHz. The reactor design features an inner stainless-steel high-voltage electrode rod encased within an outer quartz tube. A copper mesh electrode is wrapped around the quartz tube to complete the DBD configuration. All components, including the gas inlet, are assembled using a Teflon connector to ensure controlled gas delivery into the reactor. The reactor is positioned within a Venturi tube integrated into a closed-loop system to allow for continuous circulation of the aqueous solution.

Two air-feeding modes were employed: a *regulated-pressure* mode, driven passively by the negative pressure at the Venturi tube air inlet, and a *regulated-flow* mode, controlled via a mass flow controller (Alicat, USA). The voltage and current waveforms of the DBD discharge were monitored with an oscilloscope to analyze electrical characteristics and energy transfer dynamics. The temperature of the plasma discharge area was monitored using an infrared camera. The entire setup is adaptable for outdoor operation using a solar power station (Bluetti) and a diaphragm pump (Vevor) in place of the peristaltic pump (Figure S1).

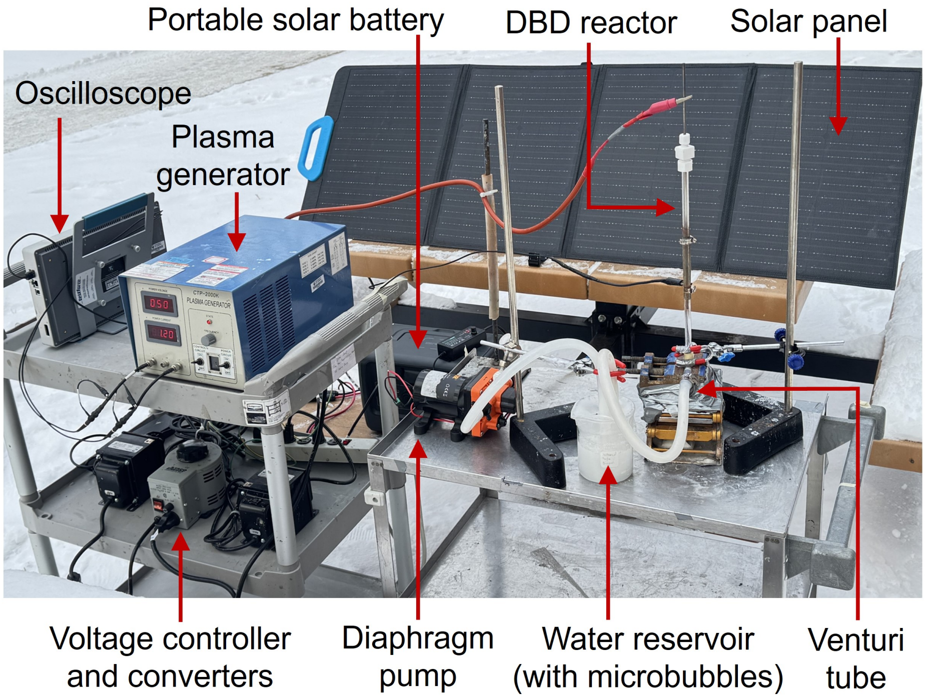

Figure S1: Photograph of the outdoor setup for the DBD MB-CPA process treating 500 mL of 0.5 M NaOH solution, driven by solar power.

The MB-CPA treatments were conducted in either pure water or NaOH solutions at varying pH levels, under a consistent liquid recirculation rate of 5 L/min and a plasma input power of 100 W. Both the regulated-pressure and regulated-flow modes were evaluated for pure water and 0.5 M NaOH solution, with the nominal air flow rate fixed at 1.55 standard liters per minute (SLM). Under the regulated-flow mode, the air-feed rate could be further manipulated between 0 and 20 SLM to investigate the influence of air residence time on nitrogen fixation efficiency. By adjusting the water reservoir, the MB-CPA platform is capable of treating aqueous volumes ranging from 0.5 L to at least 50 L. Each experimental condition was performed in triplicate to ensure consistency and repeatability of the results.

1.3 Physiochemical behavior and analytic methods

The microbubbles generated after water discharge from the Venturi tube were monitored in the water loop through a quartz tube (15 mm inner diameter) acting as an observation window. A high-speed camera (Photron FASTCAM mini) was positioned to capture the microbubbles at the cross-sectional plane of the tube, using a white light LED panel as the backlight source. Video was captured at a frame rate of 5000 fps with a resolution of 1280×1000 pixels. Fifty screenshots from the video footage for each operating condition were analyzed using ImageJ to determine the number density and individual diameter of the microbubbles.

An ORION STAR A215 pH/conductivity meter (Thermo Scientific) was used to measure pH, oxidation-reduction potential (ORP), and electrical conductivity (EC). The ${NO_2}^-$ concentration was determined using the Griess reagent method, which forms a pink-colored compound with a characteristic absorption peak at 540 nm. For analysis, 400 μL of the aqueous sample was added to a cuvette containing 400 μL of Griess reagent.[1] The mixture was shaken thoroughly and allowed to react for 15 minutes at room temperature. Subsequently, UV–vis spectroscopy (Thermo Scientific GENESYS 150) was used to measure absorbance in the 280–680 nm range. Calibration curves prepared from sodium nitrite ($NaNO_2$) standards were used to quantify the ${NO_2}^-$ concentration.[2]

Similarly, the nitrate (${NO_3}^-$) concentration was determined by UV–vis spectroscopy in the 190–300 nm range, utilizing absorption peaks at 220 nm and 275 nm. In this procedure, 20 μL of 1 M HCl was added to a 1 mL aqueous sample and allowed to react for 10 minutes. The absorbance difference ($A_{220} - A_{275}$) was calculated to correct for organic interference, and concentrations were derived from calibration curves prepared using sodium nitrate ($NaNO_3$) standards.[3]

The concentration of hydrogen peroxide (H_2O_2) was measured using the titanium(IV) oxysulfate-sulfuric acid ($TiOSO_4$) method. Here, 100 μL of $TiOSO_4$ reagent was added to 1 mL of the aqueous sample to form a yellow pertitanic acid complex. The absorbance was measured at 403 nm via UV–vis spectroscopy, and concentrations were determined using a calibration curve of known H_2O_2 standards.[4]

The emission spectrum of the DBD plasma was qualitatively assessed using optical emission spectroscopy (OES). An optical fiber spectrometer (HR4D1943, Optics Inc., USA) connected to a computer captured emissions in the 340–1020 nm range. Spectra were recorded with a resolution of 0.3 nm, averaging three scans per measurement. Peaks were identified using reference data from the NIST Atomic Spectra Database and the HITRAN database.

Radicals transported to the plasma-activated aqueous phase were detected via electron spin resonance (ESR) spectroscopy. All experiments were performed in aqueous NaOH matrices adjusted to pH 9.00 ± 0.05. Each 5 mL sample contained 0.5 mM TEMPOL as a spin probe. To differentiate radical species, specific scavengers were employed: 25 μL of catalase stock solution and 250 μL of SOD stock solution were added sequentially to the TEMPOL solution on ice prior to plasma exposure to remove reactive oxygen species (ROS). To identify reactive nitrogen species (RNS) specifically attributed to peroxynitrite ($ONOO^-$) or nitrogen dioxide ($\cdot NO_2$), 100 μL of sodium urate stock solution was added as a selective quencher. The plasma-activated air effluent was introduced into the 5 mL sample for 2 min at a gas flow rate of 1.55 SLM. Immediately after treatment, solutions were transferred to test tubes on ice for spectral analysis. ESR spectra were recorded at room temperature using an X-band spectrometer (Bruker ELEXSYS). Scans were performed from 3455 G to 3555 G with a step size of 1 G. The characteristic nitroxide triplet signal was analyzed, and the peak-to-peak amplitude (or double integral) was used to quantify TEMPOL signal intensity relative to an untreated control.

1.4 Ammonia synthesis via electrocatalysis using plasma-activated water

The Ru_xCu catalyst for ammonia synthesis was prepared from $Cu(OH)_2$ nanowire array (NWA) precursors synthesized via an anodic oxidation technique. In this process, pre-cleaned copper foam (CF) was anodized in a 2.0 M KOH solution for 2 h, with a graphite rod serving as the counter electrode. A constant current density of 5 $mA\,cm^{-2}$ was applied throughout the anodization using a DC power source. The synthesized $Cu(OH)_2$ NWAs were then washed with deionized water and soaked in a 10 mM $RuCl_3$ solution for 12 h to undergo cation exchange. After exchange, the product was dried at 70 °C in an oven for 1 h and then annealed in a flowing Ar atmosphere at 200 °C for 2 h to convert it into Ru-doped CuO NWs. Finally, an electroreduction process was conducted at a current density of 200 $mA\,cm^{-2}$ for 8 h in a 0.5 M KOH electrolyte to obtain the metallic Ru_xCu catalyst. Scanning electron microscopy (SEM, Hitachi S4800) was used to characterize the morphology and elemental composition of the synthesized catalysts.

To prepare the electrolyte, 500 mL of 0.5 M NaOH aqueous solution was treated by the DBD MB-CPA process for 10 h. The liquid recirculation rate was 5 $L\,min^{-1}$ under regulated air suction ($\sim$1.55 SLM), and the DBD plasma input power was 100 W. The concentrations of NO_2^- and NO_3^- were monitored hourly. After treatment, the plasma-activated water (PAW) was fed into an electrochemical cell for ammonia synthesis. The reduction tests were conducted using an electrochemical workstation (1470E, Solartron) with a typical three-electrode configuration in an H-type cell separated by a Nafion 211 proton exchange membrane. The setup consisted of an Hg/HgO reference electrode, a graphite rod counter electrode, and the prepared Ru_xCu catalyst as the working electrode.

Electrochemical tests were performed in the PAW (0.5 M NaOH containing plasma-generated $NaNO_3$ and $NaNO_2$) with magnetic stirring at 400 rpm. Pure Ar was continuously purged through the cathodic compartment for 1 h prior to potentiostatic testing. The potentiostatic polarization test was carried out at various potentials for 1 h. All reported potentials were converted to the reversible hydrogen electrode (RHE) scale without iR compensation using Equation (1):

$$E_{\mathrm{RHE}} = E_{\mathrm{Hg/HgO}} + 0.059 \times \mathrm{pH} \tag{1}$$

The concentration of NH_3 was determined using a modified indophenol blue method coupled with UV-vis spectroscopy. The electrolyte effluent was collected and diluted to ensure it fell within the linear detection range. A 1 mL aliquot of the diluted sample was mixed with 1 mL of 1 M NaOH containing 5 wt% salicylic acid and 5 wt% sodium citrate. Subsequently, 0.5 mL of 0.05 M NaClO solution and 0.1 mL of 1.0 wt% sodium nitroferricyanide ($C_5FeN_6Na_2O$) solution were added. The mixture was allowed to react under ambient conditions for 1 h. The absorbance of the resulting indophenol blue complex was measured using a UV–vis spectrophotometer (Hitachi U-3900H) at a wavelength of 655 nm. A standard calibration curve was established using a series of NH_4Cl solutions of known concentrations.

The NH_3 yield rate was calculated using Equation (2):

$$\text{Yield rate} = \frac{C_{\mathrm{NH_3}} \times V}{t \times S} \tag{2}$$

where $C_{\mathrm{NH_3}}$ is the concentration of NH_3(aq), V is the volume of electrolyte in the cathodic compartment (60 mL), t is the electrolysis time (1 h), and S is the geometric surface area of the catalyst (1 cm^2).

For the calculation of Faradaic Efficiency (FE) in the eNO_x^-RR, both NO_3^- and NO_2^- are present. The concentrations of NH_3 originating specifically from NO_3^- versus NO_2^- were estimated based on the consumption ratio of the reactants:

$$C_{\mathrm{NH_3\,(from\,NO_3^-)}} = \frac{C_{\mathrm{NH_3}} \times \Delta c_{\mathrm{NO_3^-}}}{\Delta c_{\mathrm{NO_3^-}} + \Delta c_{\mathrm{NO_2^-}}} \tag{3}$$

$$C_{\mathrm{NH_3\,(from\,NO_2^-)}} = \frac{C_{\mathrm{NH_3}} \times \Delta c_{\mathrm{NO_2^-}}}{\Delta c_{\mathrm{NO_3^-}} + \Delta c_{\mathrm{NO_2^-}}} \tag{4}$$

The total Faradaic efficiency (FE) was then calculated as the sum of the partial efficiencies:

$$\mathrm{FE} = \mathrm{FE}_{\mathrm{NO_2^-\to NH_3}} + \mathrm{FE}_{\mathrm{NO_3^-\to NH_3}} = \left(\frac{6FC_{\mathrm{NH_3\,(from\,NO_2^-)}}V}{M_{\mathrm{NH_3}}Q} + \frac{8FC_{\mathrm{NH_3\,(from\,NO_3^-)}}V}{M_{\mathrm{NH_3}}Q}\right) \times 100\% \tag{5}$$

where $M_{\mathrm{NH_3}}$ is the molar mass of $\mathrm{NH_3}$ ($17\,\mathrm{g\,mol^{-1}}$), F is the Faraday constant ($96{,}485\,\mathrm{C\,mol^{-1}}$), and Q is the total charge passed, obtained by integrating the i–t curve.

2. Results

2.1 Microbubble size distribution in aqueous phase

The peak microbubbles sizes obtained from the normalized size distribution under pure water, 0.1 M NaOH, and 0.5 M NaOH solution were displayed in Table S1

Table S1: Peak size of microbubbles in varying liquid media.

Liquid Medium	**Concentration (M)**	**Peak Size** (µm)
Pure Water	0.0	23.7
NaOH	0.1	75.0
NaOH	0.5	5.6

2.2 Computational fluid dynamics simulations

In this study, the commercial CFD software ANSYS Fluent 2021 R1 was employed to simulate the transport of plasma-activated gas within the DBD reactor. The multiphase flow characteristics inside the three-dimensional reactor were resolved using an Unsteady Reynolds-Averaged Navier–Stokes (URANS) framework coupled with the Realizable k–ϵ turbulence model. The compressibility of the gas phase was neglected. The Volume of Fluid (VOF) method was adopted to capture the interface between the phases.

A velocity inlet boundary condition was applied, with the inflow velocity (U) varied from 1.06 to 21.22 $\mathrm{m\,s^{-1}}$ (corresponding to $Q = 1$–$20\ \mathrm{L\,min^{-1}}$). A static pressure of $P = 90,232$ Pa was prescribed at the outlet. No-slip boundary conditions were imposed on all solid walls. The turbulence intensity and turbulence viscosity ratio were set to 0.05 and 10, respectively. The three-dimensional computational domain was discretized using a hexahedral structured mesh generated in ICEM-CFD. Grid independence was established, and a mesh consisting of 1.3 million cells was selected as the optimal grid. To ensure numerical stability and accuracy, a time step of 1×10^{-4} s was used, with 30 iterations per time step.

2.3 Short-lived excited species in the plasma discharge region

Optical emission spectroscopy (OES) results confirm the presence of short-lived reactive species within the DBD plasma. The dominant reactive nitrogen species (RNS) include excited nitrogen (N_2^*), nitrogen ions (N_2^+ and N^+), and atomic nitrogen (N) (Figure S2A). The relative signal intensity of these short-lived RNS is approximately 20-fold higher than that of short-lived reactive oxygen species (ROS), such as oxygen ions (O_2^+) and excited atomic oxygen (O^*) (Figure S2B).

The relative intensity (counts) of representative short-lived RONS in the plasma activation region is plotted against the air flow rate in Figure S2C,D. Regardless of the air feed rate into the plasma reactor, the distribution of identified reactive nitrogen and oxygen species remained invariant. Furthermore, as the air flow rate increased, the intensity of short-lived RONS remained relatively stable, demonstrating that the generation of these species is independent of the gas residence time in the discharge zone.

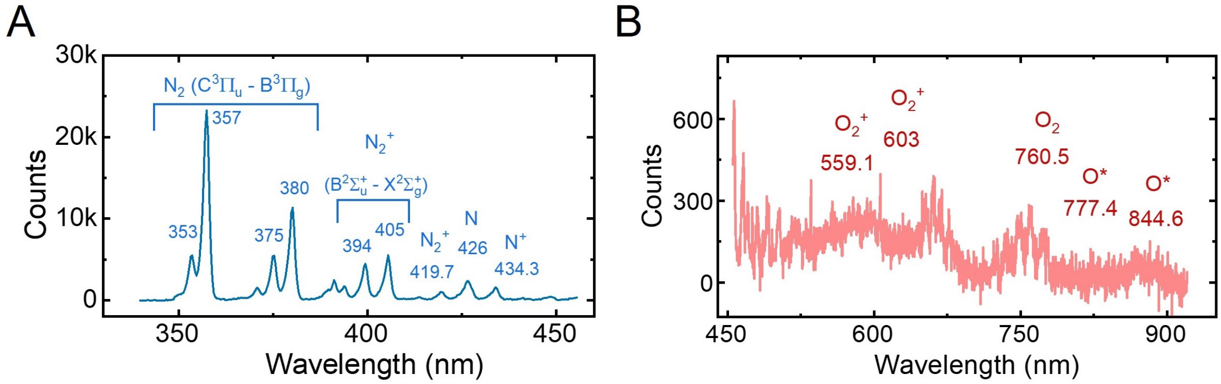

Figure S2: Optical emission spectra during plasma discharge at 100 W input power with an air-feed rate of 1.55 SLM. Spectra are shown for the wavelength ranges (A) 330 nm to 455 nm and (B) 450 nm to 920 nm.

2.3 Gas species analysis downstream of the afterglow region

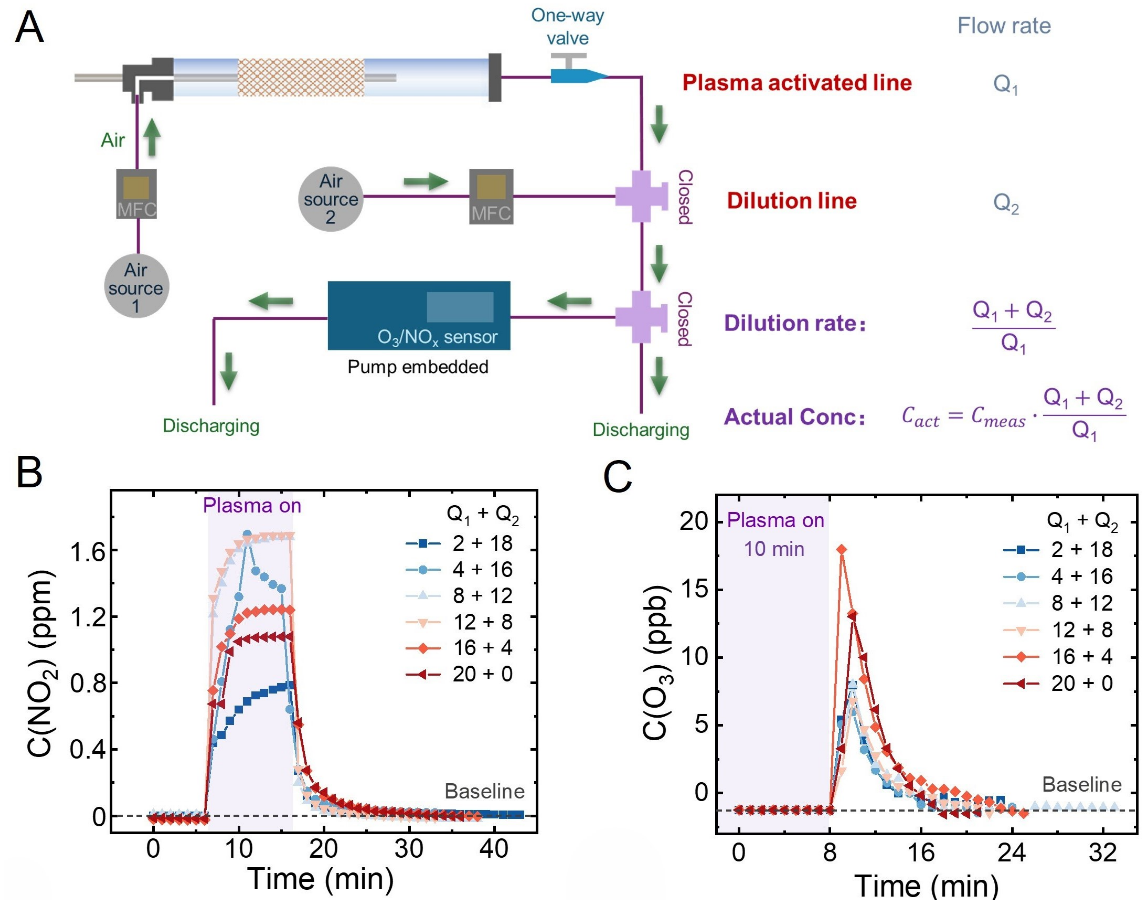

Figure S3: (A) Schematic of the gas line connection for analyzing species in the effluent of the DBD plasma reactor. (B) Measured concentrations of NO_2 and (C) ozone (O_3) using this setup.

2.4 Data points for Radar chart comparison of DBD-based technologies for NO_x^- production

The treatment volume (V, unit: mL), final NO_x^- concentration ($C(NO_x^-)_{final}$, unit: mg/L), molar production rate (R, unit: μmol/min), and specific energy cost (SEC, unit: MJ per mol of NO_x^--N) from literature (Table S2), were transformed into unified units and listed in Table S2. The normalized treated volume, final NO_x^- concentration, molar production rate was obtained by dividing the highest value as level 10. The highest value for treatment volume, final NO_x^- concentration, molar production rate are from this word under the condition of 10-h treatment of 50 L 0.5 M NaOH, 10-h treatment of 0.5 L 0.5 M NaOH, and 10-h treatment of 50 L 0.5 M NaOH, respectively.

The normalization of specific energy was conducted in a different way for better visualization (Equation (6)), making the most energy efficient method showing the highest level in the Radar chart. The minimum specific energy cost was from the work by Lamichhane et al.[5]

$$\mathrm{SEC}_{norm} = 10 - log_{10}(\frac{\mathrm{SEC}}{\mathrm{SEC}_{min}}) \tag{6}$$

Table S2: Detailed performance metrics for DBD systems, including absolute values and normalized scores for multi-axis comparison (Best absolution values were labelled by bold texts).

Ref.	**Absolute Values**				**Normalized Values**			
	V (mL)	**SEC** (MJ/mol − N)	**R** (µmol/min)	C_{final} (mg/L)	V_{norm}	SEC_{norm}	R_{norm}	$C_{final,norm}$
Lamichhane et al.[5]	40	**11.56**	0.60	12.00	0.01	9.97	0.04	0.05
Aceto et al.[6]	500	1874.88	1.34	10.00	0.10	7.76	0.08	0.04
Rathore et al.[7]	500	986.08	1.45	62.85	0.10	8.04	0.09	0.27
Pandey et al.[8]	30	442.52	1.52	45.25	0.01	8.39	0.09	0.19
Wang et al.[9]	150	15 834.67	1.71	3.47	0.03	6.84	0.11	0.01
Sun et al.[10]	200	35.45	2.20	6.82	0.04	9.49	0.14	0.03
Teng et al.[11]	30	355.65	2.41	95.00	0.01	8.49	0.15	0.40
Li et al.[12]	50	/	3.51	260.60	0.01	/	0.22	1.10
Subramanian et al.[13]	20	64.83	6.29	350.85	0.00	9.23	0.39	1.48
Yang et al.[14]	50	491.86	12.08	43.48	0.01	8.35	0.74	0.18
Wu et al.[15]	2000	370.39	16.20	27.00	0.40	8.47	1.00	0.11
Roy et al.[16]	23	13.94	21.52	580.00	0.00	9.89	1.32	2.45
Lan et al.[17]	1600	20.99	21.86	110.73	0.32	9.72	1.35	0.47
Miranda et al.[18]	40	93.05	32.70	505.00	0.01	9.07	2.01	2.13
This work (0.5 L)	500	138.95	44.67	**2367.02**	0.10	8.89	2.75	10.00
This work (50 L)	**50000**	36.93	**162.46**	123.11	10.00	9.45	10.00	0.52

References

(1) Bradu, C.; Kutasi, K.; Magureanu, M.; Puač, N.; Živković, S. Reactive nitrogen species in plasma-activated water: generation, chemistry and application in agriculture. *Journal of Physics D: Applied Physics* **2020**, *53*, 223001.

(2) Panchal, D.; Lu, Q.; Saedi, Z.; Luk, H.; Yu, T.; Zhang, X. Integrate bubble flotation and intermittent microbubble-enhanced cold plasma activation for scalable disinfection of food processing wastewater. *Separation and Purification Technology* **2025**, 131677.

(3) Lu, Q.; Panchal, D.; Yang, L.; Saedi, Z.; El-Din, M. G.; Zhang, X. Simultaneous degradation of multiple micropollutants in flowing water by mild and strong microbubble-enhanced cold plasma activation. *Water Research* **2025**, 123435.

(4) Hadinoto, K.; Astorga, J. B.; Masood, H.; Zhou, R.; Alam, D.; Cullen, P. J.; Prescott, S.; Trujillo, F. J. Efficacy optimization of plasma-activated water for food sanitization through two reactor design configurations. *Innovative Food Science & Emerging Technologies* **2021**, *74*, 102867.

(5) Lamichhane, P.; Paneru, R.; Nguyen, L. N.; Lim, J. S.; Bhartiya, P.; Adhikari, B. C.; Mumtaz, S.; Choi, E. H. Plasma-assisted nitrogen fixation in water with various metals. *Reaction Chemistry & Engineering* **2020**, *5*, 2053–2057.

(6) Aceto, D.; Rotondo, P. R.; Porfido, C.; Bottiglione, B.; Paciolla, C.; Terzano, R.; Minafra, A.; Ambrico, M.; Dilecce, G.; Leoni, B.; others Assessing plasma activated water irrigation effects on tomato seedlings. *Frontiers in Physics* **2024**, *12*, 1399910.

(7) Rathore, V.; Desai, V.; Jamnapara, N. I.; Nema, S. K. Green synthesis of ammonium nitrate (NH4NO3) fertiliser: production via plasma water/ice interaction with air and NH3 plasma. *Environmental Technology* **2025**, *46*, 2643–2655.

(8) Pandey, S.; Jangra, R.; Ahlawat, K.; Mishra, R.; Mishra, A.; Jangra, S.; Prakash, R. Selective generation of nitrate and nitrite in plasma activated water and its physico-chemical parameters analysis. *Physics Letters A* **2023**, *474*, 128832.

(9) Wang, Q.; Xin, Y.; Sun, B. Characteristics of liquid-phase continuous arc discharge plasma. *Plasma Processes and Polymers* **2022**, *19*, 2200046.

(10) Sun, J.; Zhou, R.; Hong, J.; Gao, Y.; Qu, Z.; Liu, Z.; Liu, D.; Zhang, T.; Zhou, R.; Ostrikov, K. K.; others Sustainable ammonia production via nanosecond-pulsed plasma oxidation and electrocatalytic reduction. *Applied Catalysis B: Environmental* **2024**, *342*, 123426.

(11) Teng, Y.-H.; Lin, Y.-T.; Wang, W.-H.; Liao, Y.-H. The role of O3 on the selective formation of nitrate and nitrite in plasma-treated water. *Journal of Physics D: Applied Physics* **2021**, *54*, 325203.

(12) Li, Y.; Song, Z.; Zhang, T.; Xu, W.; Ding, C.; Chen, H. Spectral Characteristics of Needle Array-Plate Dielectric Barrier Discharge Plasma and Its Activated Water. *Journal of Spectroscopy* **2021**, *2021*, 9771245.

(13) Subramanian, P. G.; Jain, A.; Shivapuji, A. M.; Sundaresan, N. R.; Dasappa, S.; Rao, L. Plasma-activated water from a dielectric barrier discharge plasma source for the selective treatment of cancer cells. *Plasma Processes and Polymers* **2020**, *17*, 1900260.

(14) Yang, X.; Zhang, Y.; Liao, H.; Tian, C.; Cui, J.; Liu, Z. Nitrogen Fixation via Catalyst-Free Water-Falling Film Dielectric Barrier Discharge Plasma: A Novel and Simple Strategy to Enhance Ammonia Selectivity. *Applied Sciences* **2025**, *15*, 1410.

(15) Wu, S.; Thapa, B.; Rivera, C.; Yuan, Y. Nitrate and nitrite fertilizer production from air and water by continuous flow liquid-phase plasma discharge. *Journal of Environmental Chemical Engineering* **2021**, *9*, 104761.

(16) Roy, N. C.; Maira, N.; Pattyn, C.; Remy, A.; Delplancke, M.-P.; Reniers, F. Mechanisms of reducing energy costs for nitrogen fixation using air-based atmospheric DBD plasmas over water in contact with the electrode. *Chemical Engineering Journal* **2023**, *461*, 141844.

(17) Lan, C.; Yin, Y.; Tan, S.; Liu, D.; Lu, X. Microbubble-enhanced plasma water-based nitrogen fixation: generation mechanisms, regulation strategies, and application prospects. *Journal of Physics D: Applied Physics* **2025**, *58*, 135203.

(18) de Souza Miranda, F.; Neto, N. F. A.; Koga-Ito, C. Y.; Pessoa, R. S. Influence of NaCl concentration on reactive species formation in plasma-activated saline solutions using coaxial DBD. *Physica Scripta* **2025**, *100*, 075611.